

# Interfacial Study To Suppress Charge Carrier Recombination for High Efficiency Perovskite Solar Cells

Nirmal Adhikari,<sup>†,||</sup> Ashish Dubey,<sup>†,||</sup> Devendra Khatiwada,<sup>†</sup> Abu Farzan Mitul,<sup>†</sup> Qi Wang,<sup>†</sup> Swaminathan Venkatesan,<sup>†</sup> Anastasiia Iefanova,<sup>†</sup> Jiantao Zai,<sup>\*,‡</sup> Xuefeng Qian,<sup>\*,‡</sup> Mukesh Kumar,<sup>§</sup> and Qiquan Qiao<sup>\*,†</sup>

<sup>†</sup>Center for Advanced Photovoltaics, Department of Electrical Engineering and Computer Science, South Dakota State University, Brookings, South Dakota 57007, United States

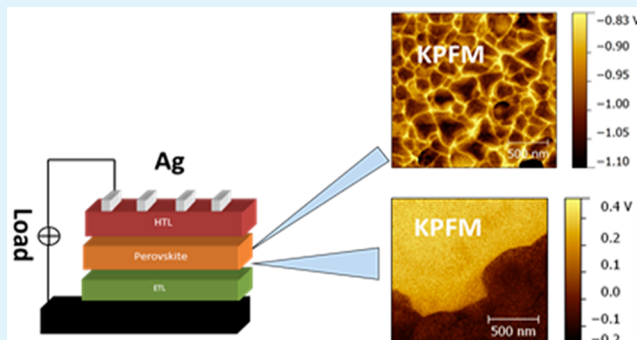
<sup>‡</sup>Shanghai Electrochemical Energy Devices Research Center, School of Chemistry and Chemical Engineering and State Key Laboratory of Metal Matrix Composites, Shanghai Jiao Tong University, Shanghai 200240, People's Republic of China

<sup>§</sup>Functional and Renewable Energy Materials Laboratory, Department of Physics, Indian Institute of Technology, Ropar, Punjab 140 001, India

## S Supporting Information

**ABSTRACT:** We report effects of an interface between TiO<sub>2</sub>–perovskite and grain–grain boundaries of perovskite films prepared by single step and sequential deposited technique using different annealing times at optimum temperature. Nanoscale kelvin probe force microscopy (KPFM) measurement shows that charge transport in a perovskite solar cell critically depends upon the annealing conditions. The KPFM results of single step and sequential deposited films show that the increase in potential barrier suppresses the back-recombination between electrons in TiO<sub>2</sub> and holes in perovskite. Spatial mapping of the surface potential within perovskite film exhibits higher positive potential at grain boundaries compared to the surface of the grains. The average grain boundary potential of 300–400 mV is obtained upon annealing for sequentially deposited films. X-ray diffraction (XRD) spectra indicate the formation of a PbI<sub>2</sub> phase upon annealing which suppresses the recombination. Transient analysis exhibits that the optimum device has higher carrier lifetime and short carrier transport time among all devices. An optimum grain boundary potential and proper band alignment between the TiO<sub>2</sub> electron transport layer (ETL) and the perovskite absorber layer help to increase the overall device performance.

**KEYWORDS:** *interface engineering, charge transport, back recombination, Kelvin probe force microscopy, perovskite film*



## 1. INTRODUCTION

Perovskite based absorbers have emerged as a promising class of materials for high efficiency solar cells.<sup>1–9</sup> Methylammonium lead trihalide perovskite materials have advantages including broad spectrum light absorption and low cost solution processing.<sup>10–14</sup> The perovskite absorber layer is a direct band gap semiconductor with large absorption coefficient ( $5.7 \times 10^4 \text{ cm}^{-1}$  at 600 nm), high carrier mobility, and long electron/hole diffusion length. These properties make perovskite a prospective candidate for the fabrication of highly efficient solar cells.<sup>15</sup>

In 2009, Miyasaka et al. made major progress by replacing the dye with methylammonium lead iodide ( $\text{CH}_3\text{NH}_3\text{PbI}_3$ ) in dye sensitized solar cells (DSCs)<sup>16,17</sup> and obtained a power conversion efficiency (PCE) of 3.8%.<sup>18</sup> Since then, a number of studies have been conducted focusing on device structure and morphological aspects.<sup>19–21</sup> An appropriate electronic band alignment between electron transport layer (ETL), hole

transport layer (HTL), and perovskite absorber layer is required to improve device performance.<sup>22</sup> The Yang group reported a record efficiency of 19.3% in lead based perovskite solar cells via interface engineering and humidity control.<sup>23</sup> Recently,  $20.1 \pm 0.4\%$  power conversion efficiency has been achieved<sup>24</sup> and outperforms other solar cells based on DSCs, CdTe, and polymer solar cells.<sup>25,26</sup> They manipulated the carrier pathways by controlling perovskite thin films, ETL, and their interfaces. Perovskite solar cells can be made in both planar and bulk heterointerface structures with high performance. More study has been done to find the best device structure in terms of robustness and stability. Therefore, deeper understanding of the electrostatic potential within the device can guide device optimization.

**Received:** July 17, 2015

**Accepted:** November 18, 2015

**Published:** November 18, 2015



Electrons need to transfer from perovskite to ETL, while holes transfer to HTL without any significant energy loss for achieving high performance solar cells.<sup>22</sup> Kelvin probe force microscopy (KPFM) is a method to determine interface energetics, which can be used for fundamental understanding to select ETL and HTL for high performance devices. Grain boundaries and grains play a critical role for perovskite solar cell performance. Grain boundary in copper indium gallium selenide (CIGS), copper–zinc–tin–sulfur/selenium (CZTS/Se), and cadmium telluride (CdTe) solar cells has been found as an important fact for high efficiency.<sup>27,28</sup> Electric field developed near grain boundaries separates the charges and enhances the collection of minority carriers, i.e., electrons in p-type absorbing materials. Furthermore, holes are repelled, and thus the recombination at the grain boundary is suppressed. Photogenerated electrons are attracted toward grain boundaries, transferred to the ETL, and finally collected to the end electrode enhancing short circuit current density of the device.<sup>29</sup> The density of states (DOS) analysis shows that GBs do not generate any deep level trap states in the bandgap of perovskite solar cells making grain boundary properties benign.<sup>5</sup>

Study shows that contact potential difference (CPD) of GBs in perovskite films is higher than within the grains and decreases after illumination. In addition, GBs potential can be controlled through passivation.<sup>6,7</sup> Recent study has shown that GBs play a beneficial role and have higher surface potential along GBs.<sup>8</sup> It has also been demonstrated from the CS-AFM measurement that higher short circuit current is collected near GBs compared to within interior grains. However, the effect on photogenerated charges at the perovskite–ETL interface and at GBs with annealing conditions remains unclear, which is one of the critical parameters to minimize carrier recombination.

In this work, we report KPFM study to quantify the barrier that prevents back-recombination between holes in perovskite and electrons in TiO<sub>2</sub> at the TiO<sub>2</sub>–perovskite interface and at the GBs within the perovskite layer at different annealing times. KPFM was used to map local electronic properties in grains and at GBs, leading to a better understanding of charge transport in perovskite solar cells. KPFM measurements showed that perovskite materials exhibit higher CPD, i.e., higher work function at GBs which is beneficial for minority charge carrier collection and can improve device performance. In addition, GB potential within the grains of the perovskite active layer at different annealing times was measured using KPFM and correlated with device performance. The role of a lead iodide capping layer on suppressing back-recombination was also investigated. The perovskite layer surface morphologies for both the single step and sequential deposition were investigated in correlation to device performance.

## 2. EXPERIMENTAL PROCEDURE

**Materials.** Methylammonium iodide (CH<sub>3</sub>NH<sub>3</sub>I) and mesoporous TiO<sub>2</sub> (Dyesol 18NRT with particle size of 20 nm) was purchased from Dyesol. PbI<sub>2</sub> was purchased from Acros Organics. FTO coated glass substrates were purchased from Hartford Glass Co.

**Device Fabrication.** Devices were fabricated on fluorine doped tin oxide (FTO) coated glass. The FTO layer was etched using zinc powder and diluted hydrochloric acid (HCl). Substrates were subsequently rinsed with DI water. All etched substrates were then cleaned by detergent water, DI water, acetone, and isopropanol by sonication for 20 min each. Substrates were then dried, followed by plasma cleaning for 20 min in the presence of oxygen.

All cleaned substrates were coated by a compact layer of TiO<sub>2</sub> from its precursor (titanium diisopropoxide bis(acetylacetone), 75 wt % solution in 2-propanol) solution of 0.15 and 0.3 M, by spin coating each layer at 4500 rpm for 30 s. A compact layer of TiO<sub>2</sub> coated substrates was then annealed at 450 °C for 30 min. The substrates were cooled to room temperature. A 1 g amount of TiO<sub>2</sub> (Dyesol 18NRT with particle size of 20 nm) was diluted with 4.436 mL of ethanol, and the mixed solution was spin coated at 5500 rpm on top of the compact layer of TiO<sub>2</sub>. The thickness of the mesoporous TiO<sub>2</sub> is approximately 600 nm. The thick substrates were annealed at 450 °C for 30 min and then cooled to room temperature. Substrates were then treated by dipping them in TiCl<sub>4</sub> (25 mM) solution for 30 min at 70 °C, followed by rinsing with DI water and ethanol and then annealed at 450 °C for 30 min. Finally, substrates were then transferred inside a glovebox for depositing the perovskite layer using a one step spin coating process and a two step sequential deposition method, respectively.

**One Step Method.** CH<sub>3</sub>NH<sub>3</sub>I (0.1975 g) and PbI<sub>2</sub> (0.5785 g) were mixed in 1 mL of  $\gamma$ -butyrolactone and stirred for 12 h. TiO<sub>2</sub> coated substrates were then spin coated with the aforementioned mixed solution at 2000 rpm for 60 s, and 3000 rpm for another 60 s, resulting in a black color film. Black color perovskite (CH<sub>3</sub>NH<sub>3</sub>PbI<sub>3</sub>) films were then annealed at 100 °C for 15, 30, and 60 min, respectively. Spiro-OMeTAD was used as a hole transport layer, which was prepared by mixing 72.3 mg of 2,2',7,7'-tetrakis(*N,N*-di-*p*-methoxyphenylamine)-9,9-spirobifluorene (spiro-MeOTAD), 28.8  $\mu$ L of 4-*tert*-butylpyridine, and 17.5  $\mu$ L of a stock solution of 520 mg/mL lithium bis(trifluoromethylsulfonyl)imide in acetonitrile in 1 mL of chlorobenzene. Spiro-OMeTAD was spin coated on top of the perovskite layer at 2000 rpm for 40 s. Silver (Ag) was then finally deposited through a mask as the top electrode in a high vacuum chamber using thermal evaporation.

**Sequential Deposition Method.** PbI<sub>2</sub> solution (462 mg/mL in DMF) was prepared by overnight stirring at 70 °C. The solution was then spin coated on top of the mesoporous TiO<sub>2</sub> layer at 6500 rpm for 90 s followed by annealing at 70 °C for 30 min. To form perovskite films, the PbI<sub>2</sub> films were prewetted in isopropanol and then dipped in CH<sub>3</sub>NH<sub>3</sub>I solution (10 mg/mL in isopropanol) for 50 s, followed by immediate spin coating at 6000 rpm for 10 s. The films were then annealed at 100 °C for different times. Spiro-OMeTAD was used as another hole transport layer, which was prepared by mixing 72.3 mg of spiro-MeOTAD, 28.8  $\mu$ L of 4-*tert*-butylpyridine, and 17.5  $\mu$ L of a stock solution of 520 mg/mL lithium bis(trifluoromethylsulfonyl)imide in acetonitrile in 1 mL of chlorobenzene. Spiro-OMeTAD was spin coated on top of the perovskite layer at 2000 rpm for 40 s. Silver (Ag) was then finally deposited as the top electrode in a high vacuum chamber using thermal evaporation.

**TiO<sub>2</sub>–Perovskite Interface.** To investigate the TiO<sub>2</sub>–perovskite interface with different annealing conditions, a thin layer of a compact layer (c-TiO<sub>2</sub>) was spin coated at 4500 rpm for 40 s and annealed at 450 °C for 30 min. Methylammonium lead iodide (CH<sub>3</sub>NH<sub>3</sub>PbI<sub>3</sub>) solution was spin coated on one corner of the TiO<sub>2</sub> film at 2000 rpm for 60 s and 3000 rpm for 60 s and annealed at 100 °C for different times with the same condition as that used for perovskite solar cell device fabrication. To form the TiO<sub>2</sub>–perovskite interface for sequential deposition technique, the PbI<sub>2</sub> films were deposited at 6500 rpm for 90 s and annealed at 70 °C for 30 min. These films were prewetted in isopropanol and then dipped in CH<sub>3</sub>NH<sub>3</sub>I solution (10 mg/mL in isopropanol) for 50 s, followed by spin coating at 6000 rpm for 10 s on top of c-TiO<sub>2</sub> immediately.

**Characterization.** An Agilent 8453 UV-vis spectrophotometer G1103A was used to measure absorbance spectra of perovskite films. X-ray diffraction (XRD) spectra were recorded from a Rigaku Smartlab system. XRD was performed outside the glovebox immediately after preparing the samples. The fabricated perovskite solar cells were characterized by current density–voltage (*J*–*V*) characteristics measured using Agilent 4155C under illumination of a solar simulator (xenon lamp, Newport) with an intensity of ~100 mW/cm<sup>2</sup> (AM 1.5). The intensity of illumination was calibrated using a National Renewable Energy Laboratory (NREL) photodector to set the

distance between the solar cell and the solar simulator. All solar cells with area  $0.16 \text{ cm}^2$  were characterized in the same conditions with  $0.5 \text{ V/s}$  scan rate in both forward and reverse scan sweeping from 0 to 1 V at a relative humidity of 40% in ambient conditions.

**Transient Measurements.** Transient photovoltage (TPV) was performed using a dye laser (532 nm) coupled with the nitrogen laser (337 nm) to create a short transient in the cell. The transient optical excitation was achieved by focusing a pump laser pulse on the device generated by an OBB's Model OL-4300 nitrogen laser (a crisp pulse at 337 nm)—Model 1011 dye laser as the excitation source (repetition rate  $\sim 4 \text{ Hz}$ ; pulse duration  $< 1 \text{ ns}$ ). The transient photovoltage was measured with a high impedance ( $1 \text{ M}\Omega$ ) of the oscilloscope to operate the device in open circuit condition. The transient photocurrent was measured with low impedance ( $50 \text{ }\Omega$ ) of the oscilloscope to operate the device in a condition that is close to the short circuit condition. The generated transients were recorded using an Agilent MSO 07034B mixed oscilloscope (350 MHz, 2 Gsa/s). The pulse width of the dye laser was measured on the oscilloscope through the response of the photodiode (rise time, less than 1 ns; spectral range, 280–1100 nm) as an excitation source to the device. The obtained data were fitted with a monoexponential decaying function to calculate the charge carrier lifetime of the devices.

**KPFM Imaging.** KPFM is a noncontact atomic force microscopy method which uses a conducting tip as a Kelvin probe to measure surface potential. It uses a feedback loop that adjusts DC potential which nullifies the force component experienced in the tip, giving rise to surface potential.<sup>29–31</sup> KPFM is an important tool to obtain a back-recombination barrier between the electron transport layer and the perovskite layer, and within the grains of the perovskite layer. The device performance in terms of energetics of the transport layers, i.e., energy positions of electronic bands and their alignment with energy levels of the perovskite layer at different annealing conditions, has been determined.

The CPD between the tip and sample was measured together with topography. The tip was excited with an electrical oscillation that induces an electrostatic force between the tip and sample. This electrostatic force was nullified by applying the direct-voltage (dc) offset on the scanning tip at every pixel on the sample. This potential is actually the CPD between the tip and sample, which is their work function difference. An Agilent SPM 5500 atomic force microscope equipped with a MAC III controller (comprising three lock-in amplifiers) was used to map surface potential at the  $\text{TiO}_2$ –perovskite interface and within the perovskite layer. A Budget Sensors Multi 7S-EG tip having a platinum/iridium conductive coating was used. The tip's first resonance ( $f_1$ ) frequency of 67 kHz was fed into the first lock-in amplifier (LIA1). The vertical tip–sample separation was controlled from LIA1 which provided the error in the amplitude signal at  $f_1$  to the servo. This first lock-in amplifier was used for topographic and phase imaging, while the second frequency ( $f_2$ ) at 5 kHz using a second lock-in amplifier (LIA2) gave KPFM measurement. LIA2 provided an electrical oscillation to the tip at 5 kHz with a certain dc offset to induce an electrostatic force between the tip and sample. This electrostatic amplitude was attained with a dc offset of  $-3 \text{ V}$ , and the drive percentage of LIA2 was approximately 15% to attain an amplitude of 0.2 V. In KPFM, an external dc servo was used that nullified the electrostatic interaction by applying a certain dc bias to the tip. This dc bias recorded at each point gave the local CPD or surface potential, and hence the images of KPFM were constructed using the pixel coordinates. Our AFM and KPFM setup is inside the glovebox. All of the KPFM measurements were carried out inside the glovebox with  $\text{O}_2$  and  $\text{H}_2\text{O}$  level  $< 0.1 \text{ ppm}$  in order to ensure that the phase of the perovskite is not affected by the moisture and oxidation that can complicate the analysis. The KPFM was done in the interface between  $\text{TiO}_2$  and  $\text{MAPbI}_3$  on planar samples. The samples were prepared by spin coating  $\text{CH}_3\text{NH}_3\text{PbI}_3$  solution on one corner of the  $\text{TiO}_2$  coated substrates. This will give a step interface between  $\text{TiO}_2$  and perovskite. To avoid the topography interference with surface potential measurement, we performed SP vs  $z$  spectroscopy. The constant SP at different  $z$  values reveals the independence of SP on surface topography.

### 3. RESULTS AND ANALYSIS

Panels a and b of Figure 1 show XRD spectra of perovskite film without annealing and with annealing at  $100^\circ\text{C}$  for 15, 30, and

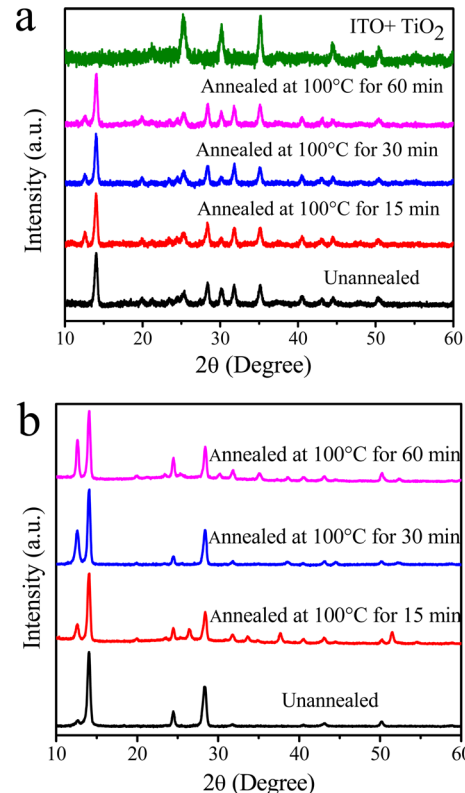


**Figure 1.** XRD spectra of perovskite films annealed at  $100^\circ\text{C}$  for different times prepared by (a) single step and (b) sequential deposition method, respectively.

60 min, respectively, by single step and sequentially deposited method. Strong peaks at  $14.09^\circ$  (110),  $28.37^\circ$  (220), and  $31.8^\circ$  (312) indicate the formation of pure perovskite ( $\text{CH}_3\text{NH}_3\text{PbI}_3$ ) phase with high crystallinity. The peak at  $12.65^\circ$  corresponds to  $\text{PbI}_2$  phase.

In the single step method, a small amount of  $\text{PbI}_2$  phase is formed upon annealing the perovskite film prepared. A  $\text{PbI}_2$  phase is formed upon annealing due to decomposition of the perovskite phase upon annealing at  $100^\circ\text{C}$ , where  $\text{CH}_3\text{NH}_3\text{I}$  escaped from the perovskite film to form  $\text{PbI}_2$ . In addition to this, the lead iodide phase in the single step method may be due to a residual phase from preparation which remains within the bulk of the material. However, a slight reduction in the  $\text{PbI}_2$  phase is found after increasing the annealing time from 15 to 30 and 60 min. This may be due to the escaping of loosely bonded  $\text{CH}_3\text{NH}_3\text{I}$  in the perovskite film from heating for longer time.

In the sequential deposition method, the XRD spectrum (Figure 1b) shows an increase in the  $\text{PbI}_2$  phase as annealing time gets longer. In sequential method, the perovskite phase ( $\text{CH}_3\text{NH}_3\text{PbI}_3$ ) forms when dipping the  $\text{PbI}_2$  layer in  $\text{CH}_3\text{NH}_3\text{I}$  solution, followed by annealing. In addition, the  $\text{PbI}_2$  layer may not be fully converted to perovskite due to incomplete conversion which is also seen in XRD spectra of the unannealed film. During the annealing,  $\text{CH}_3\text{NH}_3\text{I}$  can escape if annealed too long especially for some loosely bonded perovskite phases.<sup>7,32</sup>  $\text{PbI}_2$  resulting from decomposition of perovskite due to annealing in combination with incomplete

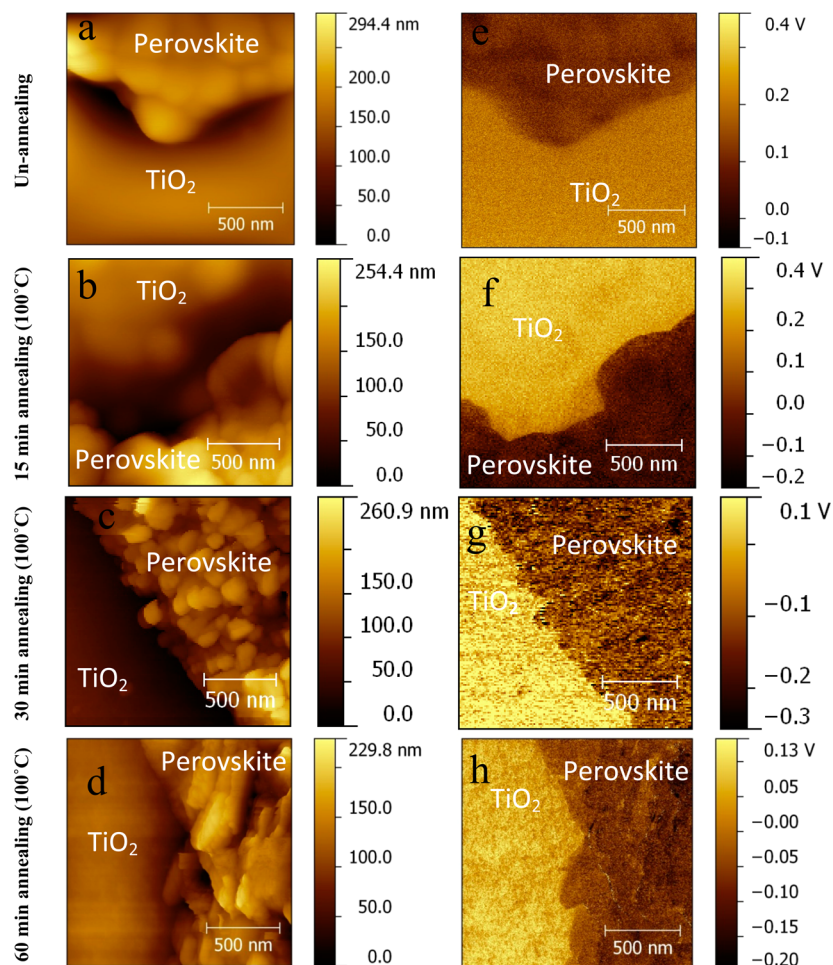


**Figure 2.** (a–d) 2D topography and (e–h) 2D surface potential of the perovskite– $\text{TiO}_2$  interface by depositing perovskite films on a  $\text{TiO}_2$  layer from the single step method without annealing and with annealing for 15, 30, and 60 min at 100 °C.

conversion of the  $\text{PbI}_2$  phase increases with increasing annealing time in sequential deposition method. However, the  $\text{PbI}_2$  phase does not change significantly in the single step method after annealing for longer time. The possible reason is that, in the single step method, two precursor solutions ( $\text{CH}_3\text{NH}_3\text{I}$  and  $\text{PbI}_2$ ) were mixed together in a single solvent so that both  $\text{CH}_3\text{NH}_3\text{I}$  and  $\text{PbI}_2$  have better contact with each other to form perovskite  $\text{CH}_3\text{NH}_3\text{PbI}_3$ . Even after perovskite  $\text{CH}_3\text{NH}_3\text{PbI}_3$  decomposes when we apply heating/annealing, they will readily re-form perovskite  $\text{CH}_3\text{NH}_3\text{PbI}_3$ .

Sequential deposition method was done by first coating the  $\text{PbI}_2$  layer and then dipping it in MAI ( $\text{CH}_3\text{NH}_3\text{I}$ ) solution to form perovskite film. This leaves some unconverted  $\text{PbI}_2$  within the bulk of the perovskite film which gives a higher content of  $\text{PbI}_2$  in sequential deposition method compared to the one step method where the two precursors, i.e.,  $\text{PbI}_2$  and MAI, are mixed together to form a homogeneous solution. This solution is spin coated to form a perovskite film which leaves a lower amount of  $\text{PbI}_2$  in the perovskite film due to complete miscibility between  $\text{PbI}_2$  and MAI.

Figure 2 shows topography and KPFM images of the  $\text{TiO}_2$ –perovskite interface prepared by depositing perovskite films on a  $\text{TiO}_2$  layer without annealing and with annealing at 100 °C for 15, 30, and 60 min, respectively. The grain size of perovskite films decreases from 200 nm for no annealing (Figure 2a) to 85–100 nm in the 30 min (Figure 2c) and 60 min (Figure 2d)

annealed films. However, grain size does not change significantly for the 15 min annealed sample (Figure 2b) at the interface between  $\text{TiO}_2$  and perovskite. Panels e–h of Figure 2 show the change of surface potential at the  $\text{TiO}_2$ –perovskite interface upon the annealing time. The dark brown region in Figure 2e–h is perovskite and the light brown is  $\text{TiO}_2$ . A higher potential was found at the  $\text{TiO}_2$  side and a lower potential at the perovskite side. The difference in surface potential between  $\text{TiO}_2$  and perovskite increases with annealing time. This is in agreement with the previously reported KPFM measurements of perovskite film which revealed the role of annealing to suppress the recombination.<sup>20</sup>

Panels a–d of Figure 3 show the line scanning profile of surface potential at the perovskite– $\text{TiO}_2$  interface. The difference in surface potential between perovskite and  $\text{TiO}_2$  is the energy barrier that an electron from  $\text{TiO}_2$  and a hole from perovskite need to overcome for recombination. As the annealing time increases from no annealing to 15, 30, and 60 min of annealing at 100 °C, the back-recombination barrier increases. Table 1 summarizes the values of the back-recombination barrier at the  $\text{TiO}_2$ –perovskite interface for different annealing times. For unannealed samples, KPFM measurements reveal an energy barrier of 0.122 eV (Figure 3a) between  $\text{TiO}_2$  and perovskite. When annealed at 100 °C for 15, 30, and 60 min using the single step method, KPFM measurements exhibit that the back-recombination barrier

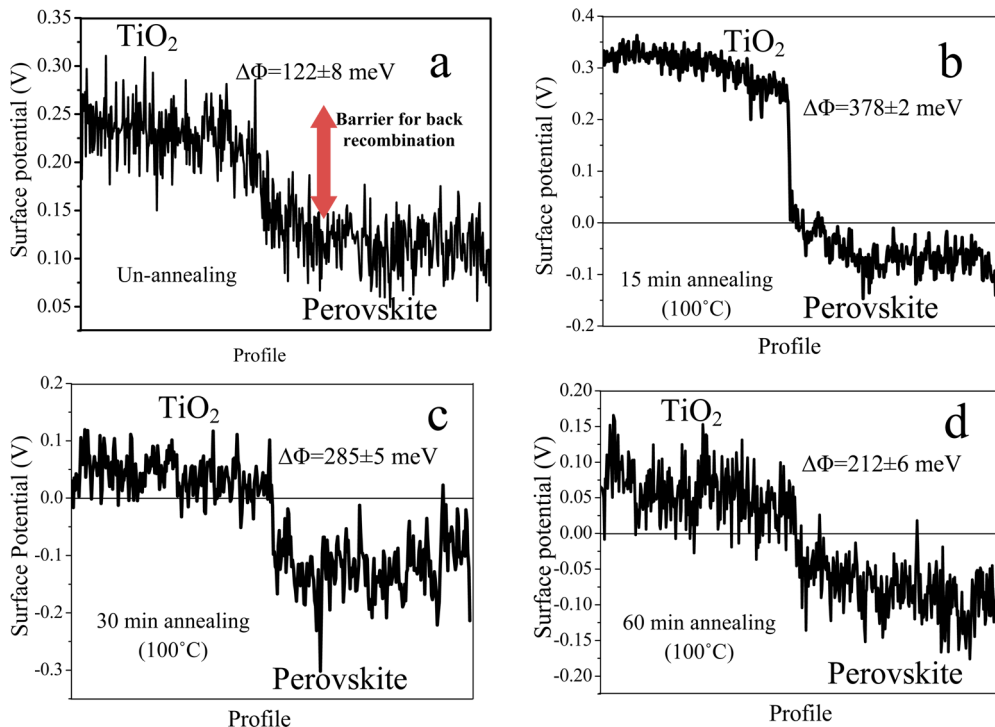


**Figure 3.** Surface potential line profiles across the perovskite– $\text{TiO}_2$  interface from the single step method for (a) no annealing and (b) 15 min, (c) 30 min, and (d) 60 min annealing at 100 °C.

**Table 1. Energetic Barriers for Back-recombination between Holes in a Perovskite Layer and Electrons in an ETL Layer Measured by KPFM<sup>a</sup>**

perovskite film	energetic barriers for back-recombination (eV)
unannealed	$0.122 \pm 0.008$
15 min annealing	$0.378 \pm 0.002$
30 min annealing	$0.285 \pm 0.005$
60 min annealing	$0.212 \pm 0.005$

<sup>a</sup>The films were prepared from the single step method annealed at 100 °C for different times.

between  $\text{TiO}_2$  and perovskite increases to 0.378 eV (Figure 3b), 0.285 eV (Figure 3c), and 0.212 eV (Figure 3d), respectively. This is much higher than 0.122 eV for unannealed samples. Such increased barriers upon annealing become more significant in preventing the back-recombination between electrons from  $\text{TiO}_2$  and holes from perovskite. This is also supported by the  $JV$  curves as open circuit voltage ( $V_{oc}$ ) increases significantly after annealing (Supporting Information Figure S4 and Table S2). The XRD spectra in Figure 1a suggest that the annealing processing helps form a thin layer of lead iodide. This  $\text{PbI}_2$  layer increases the back-recombination barrier, which was reported previously.<sup>7</sup> This is further confirmed by measuring the  $\text{TiO}_2$  – perovskite interface from the sequential deposition method and will be discussed later.

Figure 4 shows the surface potential distribution of perovskite film unannealed and annealed at 100 °C for 15, 30, and 60 min using the single step method. The surface potential distributions were acquired from KPFM images shown in Figure S2 (Supporting Information). The surface potential of perovskite films annealed at 100 °C for 15, 30, and 60 min were higher compared to the unannealed sample. The surface potential of perovskite film annealed at 100 °C for 15

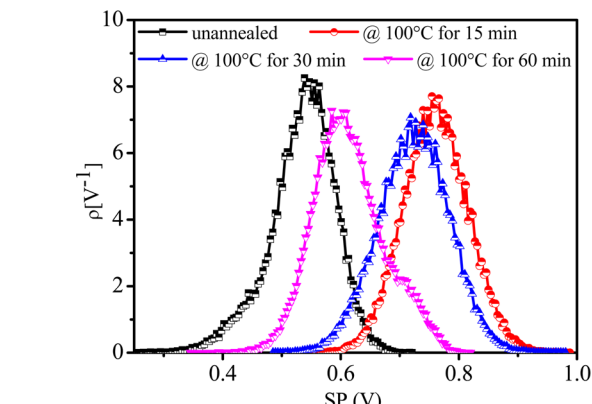


**Figure 4.** Surface potential distribution of perovskite films prepared by the single step method at different conditions of no annealing and annealing at 100 °C for 15, 30, and 60 min.

min shows the highest surface potential which is mainly due to reduced surface defects caused by the dangling bonds. These dangling bonds act as a trap center for electrons. It is reported that the origin of dangling bonds is due to the exposed iodine atoms in the perovskite film.<sup>33</sup> It is found that annealing the film at 100 °C for 15 min helps for reconstruction of the perovskite surface reducing the structural defects in the surface. In addition, the reduced surface defects which act as electron traps also reduce hysteresis of the prepared device as surface trap states are considered as one of the sources for the origin of the hysteresis. The decrease in potential for the perovskite film annealed for a longer time than 15 min can be attributed to the formation of surface defects from vacancies and intrinsic defect doping due to long term thermal annealing.<sup>34</sup>

Panels a–d of Figure 5 show 2D surface topography of perovskite films without annealing and with annealing at 100

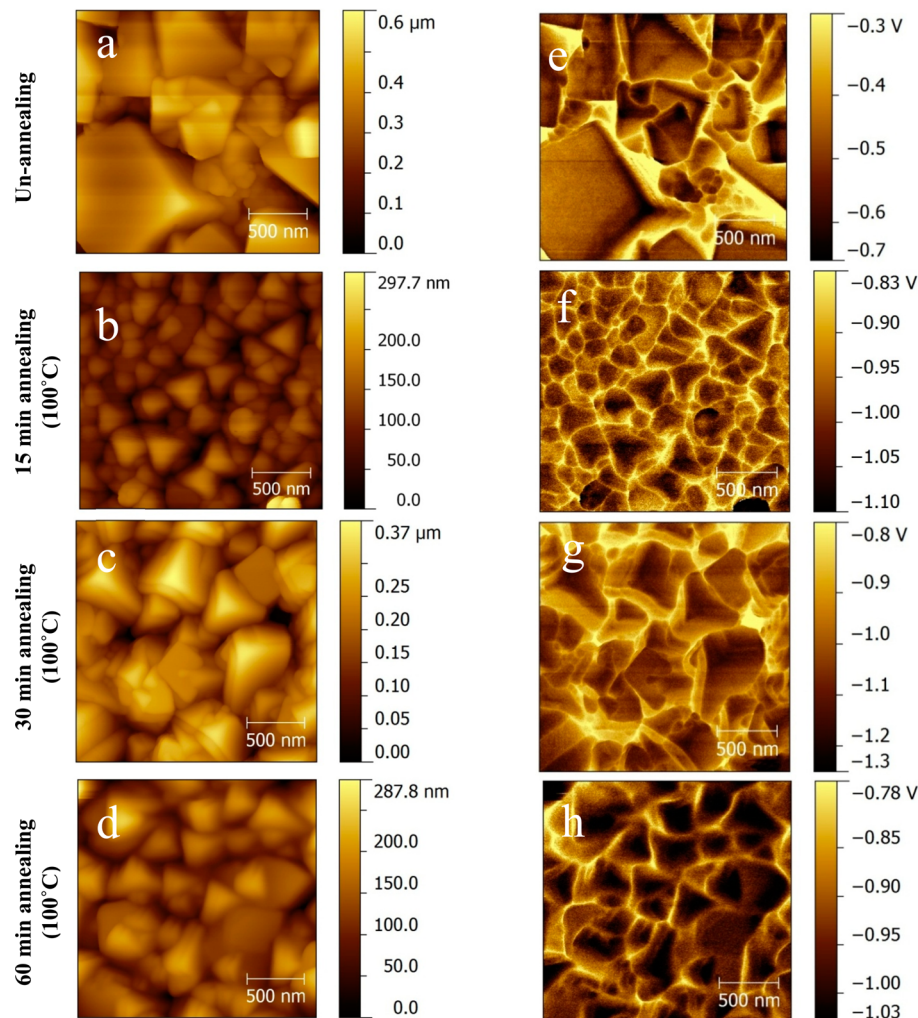


**Figure 5.** (a–d) 2D topography and (e–h) 2D surface potential images of perovskite films prepared by sequential deposition method at different conditions of no annealing and annealing at 100 °C for 15, 30, and 60 min.

°C for 15, 30, and 60 min, respectively from sequential deposition. The unannealed films show larger grains with 500–800 nm in size as shown in Figure 5a. Annealing of perovskite films led to fast evaporation of solvent molecules in the film and fast crystallization of perovskite films. This results in small particle size. However, the perovskite film without annealing forms the perovskite crystal with slower interdiffusion of PbI<sub>2</sub> and MAI, whereas the annealed films form the perovskite crystal instantaneously due to thermal annealing leaving solvent to evaporate immediately. This led to slow crystallization of perovskite phase because the residual solvent molecules assisted the interdiffusion of PbI<sub>2</sub> and MAI components to each other, leading to formation of large particles. The grain size decreases to ~75–250 nm upon annealing the perovskite film at 100 °C for 15 min. However, the grain size remains similar after annealing at 100 °C for 30 min. A slight increase in grain size (250–400 nm) was found after longer annealing time (100 °C for 60 min). It is found that the film annealed at 100 °C for 15 min has a compact and closely packed surface topography. Panels e–h of Figure 5 show 2D surface potential maps of perovskite films without annealing and with annealing at 100 °C for 15, 30, and 60 min, respectively. KPFM of perovskite films demonstrates a higher surface potential at the grain boundaries (GBs) than within grains. This corresponds to a

downward band bending in the energy band diagram leading to the minority carriers electrons in p-type absorber layer to be attracted toward GBs.<sup>27,29,35</sup> It has been shown that the grain boundary in this type of material enhances minority carrier collection, provides a current path for minority carriers to reach the n-type layers, and enhances the overall performance of the device leading to better charge transport suppressing recombination.

Table 2 summarizes the average grain boundary potential for perovskite film without annealing and with annealing at 100 °C for 15, 30, and 60 min, respectively. The grain boundary potential decreases from 479 to 337 meV from the unannealed sample to the annealed sample at 100 °C for 15 min. However, the grain boundary potential increases to 395 and 386 meV

**Table 2. Average Grain Boundary Potential of Perovskite Films Prepared from Sequential Deposition Method Annealed at 100 °C for Different Times**

perovskite film	av grain boundary potential (meV)
unannealed	479
15 min annealing	337
30 min annealing	395
60 min annealing	386

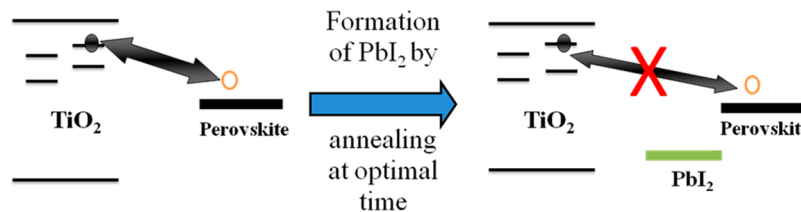


**Figure 6.** Formation of  $\text{PbI}_2$  which prevents back-recombination between electrons from  $\text{TiO}_2$  and holes from perovskite.

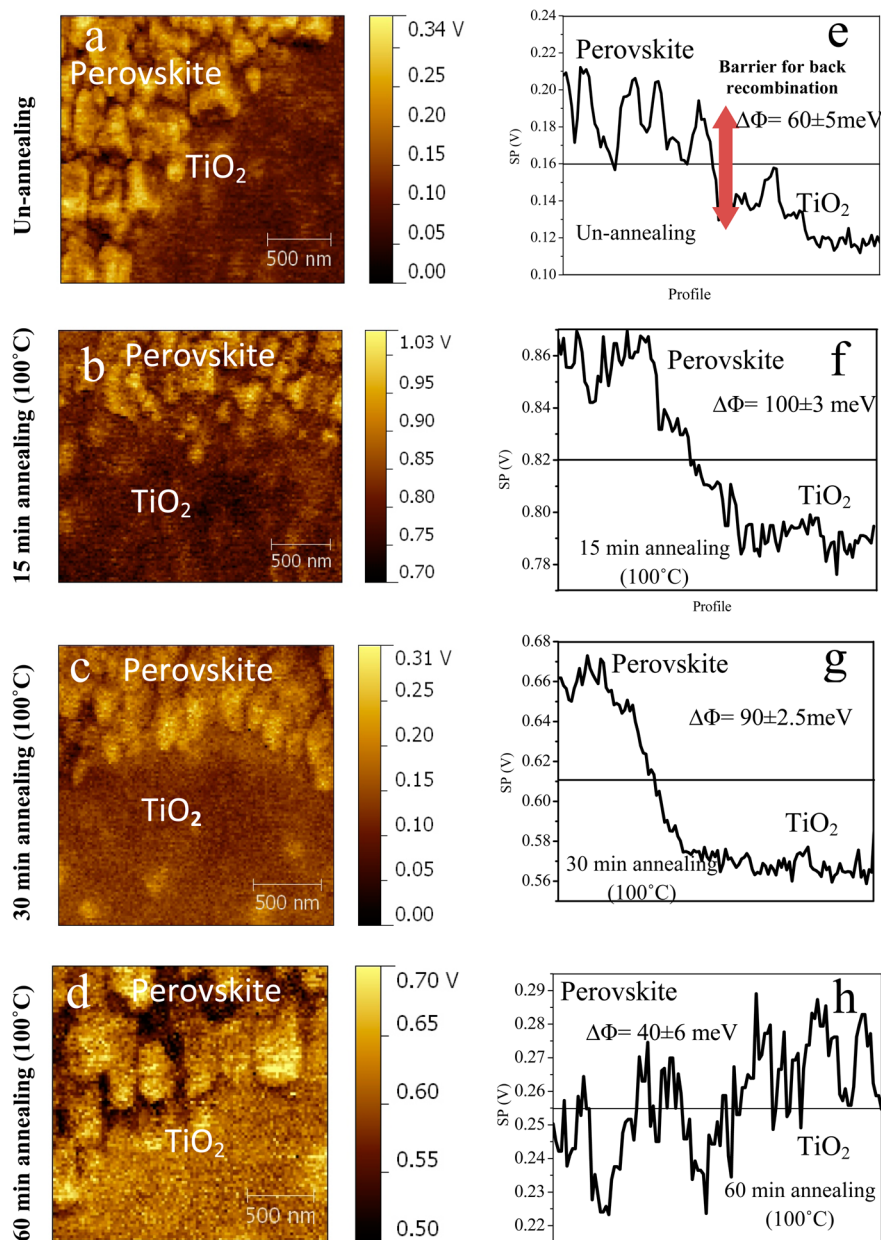


**Figure 7.** (a–d) 2D surface potential mapping and (e–h) surface potential line profile of the perovskite– $\text{TiO}_2$  interface by depositing perovskite films on a  $\text{TiO}_2$  layer from the sequential deposition method without annealing and with annealing for 15, 30, and 60 min at 100 °C.

when the sample is annealed at 100 °C for 30 and 60 min, respectively. The decrease in grain boundary potential helps to charge transport within the grains of the perovskite film by reducing the barrier between GBs. This decrease in grain boundary potential may be due to the formation of  $\text{PbI}_2$  upon annealing at 100 °C for 15 min as shown from the XRD spectrum in Figure 1b. Sequential deposition method will leave

some  $\text{PbI}_2$  together with  $\text{MAPbI}_3$ . A small amount of  $\text{PbI}_2$  is helpful for decreasing the recombination providing the beneficial role. This is one of the reasons for the lowest grain boundary potential for perovskite film annealed at 100 °C for 15 min. However, further increasing the annealing time led to formation of  $\text{MAPbI}_3$  grains with more  $\text{PbI}_2$  shells which increase the intergrain boundary potential reducing the charge

transport. Grain boundary has vacancies and interstitials, and the polarity of the grain boundary may be different with grain interiors. In addition, the grain boundary in perovskite oxides is found to be depleted and forms space charge regions due to formation of oxygen vacancies at the grain boundary.<sup>8</sup> Grain boundary potential decreases by 142 mV upon annealing for the perovskite film annealed at 100 °C for 15 min with respect to unannealed samples.

Figure 6 shows the schematic of the role of lead iodide to reduce the recombination between electrons from TiO<sub>2</sub> and holes from perovskite. An optimum amount of PbI<sub>2</sub> will reduce recombination of electrons from TiO<sub>2</sub> and holes from the perovskite layer by the introduction of lead iodide between TiO<sub>2</sub> and perovskite. TiO<sub>2</sub> has dominating surface defects (Ti<sup>3+</sup> sites) at approximately 5.0 eV which act as deep electron-donating sites. Thus, the probability of recombining electrons from TiO<sub>2</sub> and holes from perovskite with energy level 5.43 eV is higher due to energy matching. Therefore, the wide band gap PbI<sub>2</sub> helps to reduce the recombination at the interface. Thus, the highest back-recombination barrier obtained for perovskite film annealed at 100 °C for 15 min can be attributed to formation during annealing. This is in agreement with the charge transport time and charge carrier lifetime obtained from transient measurement. The perovskite film annealed at 100 °C for 15 min has fastest charge transport and longer carrier lifetime than an unannealed sample (*Supporting Information* Figure S5 and Table S3). We have found that the back-recombination decreases with an optimum content of PbI<sub>2</sub> in the perovskite film which corresponds to annealing at 100 °C for 15 min for both the single step and sequential deposition methods. The inter-grain-boundary potential was found to be a minimum for perovskite film annealed at 100 °C for 15 min. So, we conclude that a small amount of lead iodide helps to reduce recombination and increase open circuit voltage and charge transport. Therefore, the optimum amount of PbI<sub>2</sub> at perovskite–TiO<sub>2</sub> is critical because an excess amount of PbI<sub>2</sub> may partially block the electron transport because of a wide band gap.

Panels a–d of Figure 7 show 2D SP images, and panels e–h represent the line scanning profile of the surface potential at the perovskite–TiO<sub>2</sub> interface from the sequential deposition method. The largest difference in surface potential between perovskite and TiO<sub>2</sub> for film annealed at 100 °C for 15 min (Figure 7b) may be caused by the passivation of the perovskite defect states due to formation of PbI<sub>2</sub> as shown from XRD (Figure 1b). The back-recombination barrier is the difference in surface potential between perovskite and TiO<sub>2</sub>. As the annealing time increases, the back-recombination barrier for 15, 30, and 60 min at 100 °C, increases with respect to the unannealed sample. This helps to increase  $V_{oc}$  after annealing (*Supporting Information* Figure S3 and Table S1). However, it is interesting to note that the difference in surface potential between perovskite and TiO<sub>2</sub> becomes minimal after annealing for a longer time. This may be due to the formation of a more than 50% PbI<sub>2</sub> phase as shown from the XRD spectrum. Therefore, an optimum amount of lead iodide helps to reduce the back-recombination of holes from perovskite to electrons from TiO<sub>2</sub>. An excess amount of PbI<sub>2</sub> can cause an additional blockade for electrons from perovskite to move to TiO<sub>2</sub> due to its wide band gap. Table 3 summarizes the values of the back-recombination barrier at the TiO<sub>2</sub>–perovskite interface for different annealing times. For unannealed samples, KPFM measurements reveal an energy barrier of 0.060 eV (Figure 7a)

**Table 3. Energetic Barriers for Back-recombination between Holes in a Perovskite Layer and Electrons in an ETL Layer Measured by KPFM<sup>a</sup>**

perovskite film	energetic barriers for back-recombination (eV)
unannealed	0.060 ± 0.0005
15 min annealing	0.100 ± 0.0003
30 min annealing	0.090 ± 0.00025
60 min annealing	0.040 ± 0.0006

<sup>a</sup>The films were prepared from the sequential method annealed at 100 °C for different times.

between TiO<sub>2</sub> and perovskite. When annealed at 100 °C for 15, 30, and 60 min using the sequential deposition method, KPFM measurements exhibit that the back-recombination barrier between TiO<sub>2</sub> and perovskite increases to 0.100 eV (Figure 7b) and 0.090 eV (Figure 7c) and then decreases to 0.040 eV (Figure 7d), respectively. Therefore, the optimum annealing time of 15 min at 100 °C has significant barriers to prevent the back-recombination between electrons from TiO<sub>2</sub> and holes from perovskite. This will help to increase  $V_{oc}$  of the device after annealing.

The JV curves of the sequential deposition method (*Supporting Information* Figure S3) and single step method (*Supporting Information* Figure S4) give the highest device performance for perovskite films annealed at 100 °C for 15 min. *Supporting Information* Tables S1 and S2 show that the increase in efficiency is mainly due to improvement in  $J_{sc}$  and  $V_{oc}$ . An increase in  $V_{oc}$  is due to a decrease in recombination as the back-recombination barrier increases from 0.122 to 0.378 eV for the single step method and from 0.06 to 0.10 eV for the sequential deposition method. This increase in barrier reduces the recombination of electrons from TiO<sub>2</sub> and holes from the perovskite layer by the introduction of lead iodide between TiO<sub>2</sub> and perovskite. One of the reasons for increased  $J_{sc}$  upon annealing may be the improved charge transport caused by the decrease in grain boundary potential between the grains from 0.479 eV for unannealed films to 0.337 eV in 15 min for annealed films. However, when further increasing the annealing time to 30 and 60 min, the grain boundary potential increases to 0.395 and 0.386 eV, respectively. This caused the decrease of solar cell performance when increasing the annealing time to 30 and 60 min.

#### 4. CONCLUSIONS

We have performed quantitative measurement of grain boundary (GB) potential and TiO<sub>2</sub>–perovskite interface surface potential in perovskite solar cells. Nanoscale kelvin probe force microscopy (KPFM) measurement shows that charge transport in perovskite solar cell depends upon annealing conditions. The KPFM results of single step and sequentially deposited films show that the barrier increases due to the formation of PbI<sub>2</sub> that suppresses the back-recombination between electrons in TiO<sub>2</sub> and holes in perovskite. XRD results confirm the formation of perovskite and lead iodide phase upon annealing. Surface potential spatial maps of perovskite absorber layer show a higher surface potential at GBs than within grains. Grain boundary potential was also found to decrease from no annealing to 15 min annealing, then increases with longer annealing time at 30 and 60 min. Transient photovoltaic measurement results show charge carrier lifetime is the longest at 40 μs for 15 min annealing at 100 °C and then decreases with longer annealing time.

## ASSOCIATED CONTENT

### Supporting Information

The Supporting Information is available free of charge on the ACS Publications website at DOI: [10.1021/acsami.5b09797](https://doi.org/10.1021/acsami.5b09797).

SEM images of perovskite films from single step method and sequential deposition method that were not annealed and annealed for 15 min at 100 °C, AFM topography and surface potential images of perovskite films prepared by single step method at different conditions of no annealing and annealing at 100 °C for 15, 30, and 60 min, *J*–*V* characteristics of perovskite solar cells, and transient photovoltage decay and transient photocurrent decay of perovskite solar cells from sequential deposition method ([PDF](#))

## AUTHOR INFORMATION

### Corresponding Authors

\*(Q.Q.) E-mail: [qiquan.qiao@sdstate.edu](mailto:qiquan.qiao@sdstate.edu).

\*(X.Q.) E-mail: [xfqian@sjtu.edu.cn](mailto:xfqian@sjtu.edu.cn).

\*(J.Z.) E-mail: [zaijiantao@sjtu.edu.cn](mailto:zaijiantao@sjtu.edu.cn).

### Author Contributions

†N.A. and A.D. contributed equally

### Notes

The authors declare no competing financial interest.

## ACKNOWLEDGMENTS

This research benefited from funding including from NASA EPSCoR (Grant NNX13AD31A), Pakistan-U.S. Science and Technology Cooperation Program, NSF MRI (Grant Nos. 1229577 and 1428992), and Science and Technology Commission of Shanghai Municipality (Grant 15520720900).

## REFERENCES

- (1) Schulz, P.; Edri, E.; Kirmayer, S.; Hodes, G.; Cahen, D.; Kahn, A. Interface energetics in organo-metal halide perovskite-based photovoltaic cells. *Energy Environ. Sci.* **2014**, *7*, 1377–1381.
- (2) Mitzi, D. B. Synthesis, Structure, and Properties of Organic-Inorganic Perovskites and Related Materials. *Prog. Inorg. Chem.* **1999**, *48*, 1–121.
- (3) Baikie, T.; Fang, Y.; Kadro, J. M.; Schreyer, M.; Wei, F.; Mhaisalkar, S. G.; Graetzel, M.; White, T. J. Synthesis and crystal chemistry of the hybrid perovskite (CH<sub>3</sub>NH<sub>3</sub>)PbI<sub>3</sub> for solid-state sensitised solar cell applications. *J. Mater. Chem. A* **2013**, *1*, 5628–5641.
- (4) Grätzel, M. The light and shade of perovskite solar cells. *Nat. Mater.* **2014**, *13*, 838–842.
- (5) Snaith, H. J. How should you measure your excitonic solar cells? *Energy Environ. Sci.* **2012**, *5*, 6513–6520.
- (6) Snaith, H. J. The perils of solar cell efficiency measurements. *Nat. Photonics* **2012**, *6*, 337–340.
- (7) Snaith, H. J.; Abate, A.; Ball, J. M.; Eperon, G. E.; Leijtens, T.; Noel, N. K.; Stranks, S. D.; Wang, J. T.-W.; Wojciechowski, K.; Zhang, W. Anomalous Hysteresis in Perovskite Solar Cells. *J. Phys. Chem. Lett.* **2014**, *5*, 1511–1515.
- (8) Tress, W.; Marinova, N.; Moehl, T.; Zakeeruddin, S. M.; Nazeeruddin, M. K.; Gratzel, M. Understanding the rate-dependent J-V hysteresis, slow time component, and aging in CH<sub>3</sub>NH<sub>3</sub>PbI<sub>3</sub> perovskite solar cells: the role of a compensated electric field. *Energy Environ. Sci.* **2015**, *8*, 995–1004.
- (9) Unger, E. L.; Hoke, E. T.; Bailie, C. D.; Nguyen, W. H.; Bowring, A. R.; Heumuller, T.; Christoforo, M. G.; McGehee, M. D. Hysteresis and transient behavior in current-voltage measurements of hybrid-perovskite absorber solar cells. *Energy Environ. Sci.* **2014**, *7*, 3690–3698.
- (10) Wehrenfennig, C.; Eperon, G. E.; Johnston, M. B.; Snaith, H. J.; Herz, L. M. High charge carrier mobilities and lifetimes in organolead trihalide perovskites. *Adv. Mater.* **2014**, *26*, 1584–1589.
- (11) Noh, J. H.; Im, S. H.; Heo, J. H.; Mandal, T. N.; Seok, S. I. Chemical management for colorful, efficient, and stable inorganic–organic hybrid nanostructured solar cells. *Nano Lett.* **2013**, *13*, 1764–1769.
- (12) Ball, J. M.; Lee, M. M.; Hey, A.; Snaith, H. J. Low-temperature processed meso-superstructured to thin-film perovskite solar cells. *Energy Environ. Sci.* **2013**, *6*, 1739–1743.
- (13) Eperon, G. E.; Burlakov, V. M.; Docampo, P.; Goriely, A.; Snaith, H. J. Morphological Control for High Performance, Solution-Processed Planar Heterojunction Perovskite Solar Cells. *Adv. Funct. Mater.* **2014**, *24*, 151–157.
- (14) Khatiwada, D.; Venkatesan, S.; Adhikari, N.; Dubey, A.; Mitul, A. F.; Mohammad, L.; Iefanova, A.; Darling, S. B.; Qiao, Q. Efficient Perovskite Solar Cells by Temperature Control in Single and Mixed Halide Precursor Solutions and Films. *J. Phys. Chem. C* **2015**, *119*, 25747.
- (15) Laban, W. A.; Etgar, L. Depleted hole conductor-free lead halide iodide heterojunction solar cells. *Energy Environ. Sci.* **2013**, *6*, 3249–3253.
- (16) Elbohy, H.; Thapa, A.; Poudel, P.; Adhikary, N.; Venkatesan, S.; Qiao, Q. Vanadium oxide as new charge recombination blocking layer for high efficiency dye-sensitized solar cells. *Nano Energy* **2015**, *13*, 368–375.
- (17) Thapa, A.; Zai, J.; Elbohy, H.; Poudel, P.; Adhikary, N.; Qian, X.; Qiao, Q. TiO<sub>2</sub> coated urchin-like SnO<sub>2</sub> microspheres for efficient dye-sensitized solar cells. *Nano Res.* **2014**, *7*, 1154–1163.
- (18) Kojima, A.; Teshima, K.; Shirai, Y.; Miyasaka, T. Organometal halide perovskites as visible-light sensitizers for photovoltaic cells. *J. Am. Chem. Soc.* **2009**, *131*, 6050–6051.
- (19) Nanova, D.; Kast, A. K.; Pfannmöller, M.; Müller, C.; Veith, L.; Wacker, I.; Agari, M.; Hermes, W.; Erk, P.; Kowalsky, W.; Schröder, R. R.; Lovrinčić, R. Unraveling the Nanoscale Morphologies of Mesoporous Perovskite Solar Cells and Their Correlation to Device Performance. *Nano Lett.* **2014**, *14*, 2735–2740.
- (20) Bi, D.; El-Zohry, A. M.; Hagfeldt, A.; Boschloo, G. Improved Morphology Control Using a Modified Two-Step Method for Efficient Perovskite Solar Cells. *ACS Appl. Mater. Interfaces* **2014**, *6*, 18751–18757.
- (21) Im, J.-H.; Jang, I.-H.; Pellet, N.; Grätzel, M.; Park, N.-G. Growth of CH<sub>3</sub>NH<sub>3</sub>PbI<sub>3</sub> cuboids with controlled size for high-efficiency perovskite solar cells. *Nat. Nanotechnol.* **2014**, *9*, 927–932.
- (22) Glatzel, T.; Marrón, D. F.; Schedel-Niedrig, T.; Sadewasser, S.; Lux-Steiner, M. C. CuGaSe<sub>2</sub> solar cell cross section studied by Kelvin probe force microscopy in ultrahigh vacuum. *Appl. Phys. Lett.* **2002**, *81*, 2017–2019.
- (23) Eperon, G. E.; Burlakov, V. M.; Docampo, P.; Goriely, A.; Snaith, H. J. Morphological Control for High Performance, Solution-Processed Planar Heterojunction Perovskite Solar Cells. *Adv. Funct. Mater.* **2014**, *24*, 151–157.
- (24) Green, M. A.; Emery, K.; Hishikawa, Y.; Warta, W.; Dunlop, E. D. Solar cell efficiency tables (Version 45). *Prog. Photovoltaics* **2015**, *23*, 1–9.
- (25) Adhikari, N.; Khatiwada, D.; Dubey, A.; Qiao, Q. Device and morphological engineering of organic solar cells for enhanced charge transport and photovoltaic performance. *J. Photonics Energy* **2015**, *5*, 057207.
- (26) Mitul, A. F.; Mohammad, L.; Venkatesan, S.; Adhikari, N.; Sigdel, S.; Wang, Q.; Dubey, A.; Khatiwada, D.; Qiao, Q. Low temperature efficient interconnecting layer for tandem polymer solar cells. *Nano Energy* **2015**, *11*, 56–63.
- (27) Kumar, M.; Dubey, A.; Adhikari, N.; Venkatesan, S.; Qiao, Q. Strategic review of secondary phases, defects and defect-complexes in kesterite CZTS–Se solar cells. *Energy Environ. Sci.* **2015**, *8*, 3134–3159.
- (28) Adhikari, N.; Bereznay, S.; Laes, K.; Kois, J.; Volobujeva, O.; Raadik, T.; Traksmaa, R.; Tverjanovich, A.; Öpik, A.; Mellikov, E.

High-Vacuum Evaporation of n-CuIn<sub>3</sub>Se<sub>5</sub> Photoabsorber Films for Hybrid PV Structures. *J. Electron. Mater.* **2011**, *40*, 2374–2381.

(29) Li, J. B.; Chawla, V.; Clemens, B. M. Investigating the role of grain boundaries in CZTS and CZTSSe thin film solar cells with scanning probe microscopy. *Adv. Mater.* **2012**, *24*, 720–723.

(30) Sadewasser, S.; Glatzel, T., Eds. *Kelvin probe force microscopy*; Springer: Berlin, 2012.

(31) Venkatesan, S.; Adhikari, N.; Chen, J.; Ngo, E. C.; Dubey, A.; Galipeau, D. W.; Qiao, Q. Interplay of nanoscale domain purity and size on charge transport and recombination dynamics in polymer solar cells. *Nanoscale* **2014**, *6*, 1011–1019.

(32) Chen, Q.; Zhou, H.; Hong, Z.; Luo, S.; Duan, H.-S.; Wang, H.-H.; Liu, Y.; Li, G.; Yang, Y. Planar heterojunction perovskite solar cells via vapor-assisted solution process. *J. Am. Chem. Soc.* **2014**, *136*, 622–625.

(33) Cui, P.; Fu, P.; Wei, D.; Li, M.; Song, D.; Yue, X.; Li, Y.; Zhang, Z.; Li, Y.; Mbengue, J. M. Reduced surface defects of organometallic perovskite by thermal annealing for highly efficient perovskite solar cells. *RSC Adv.* **2015**, *5*, 75622–75629.

(34) Yin, W.-J.; Shi, T.; Yan, Y. Unusual defect physics in CH<sub>3</sub>NH<sub>3</sub>PbI<sub>3</sub> perovskite solar cell absorber. *Appl. Phys. Lett.* **2014**, *104*, 063903.

(35) Seto, J. Y. The electrical properties of polycrystalline silicon films. *J. Appl. Phys.* **1975**, *46*, 5247–5254.